Spiral vortices and Taylor vortices in the annulus between rotating cylinders and the effect of an axial flow

Ch. Hoffmann, M. Lücke, and A. Pinter
Institut für Theoretische Physik, Universität des Saarlandes, D-66041 Saarbrücken, Germany
(Received 1 July 2003; published 25 May 2004)

We present numerical simulations of vortices that appear via primary bifurcations out of the unstructured circular Couette flow in the Taylor-Couette system with counter rotating as well as with corotating cylinders. The full, time dependent Navier Stokes equations are solved with a combination of a finite difference and a Galerkin method for a fixed axial periodicity length of the vortex patterns and for a finite system of aspect ratio 12 with rigid nonrotating ends in a setup with radius ratio $\eta=0.5$. Differences in structure, dynamics, symmetry properties, bifurcation, and stability behavior between spiral vortices with azimuthal wave numbers $M=\pm 1$ and $M=0$ Taylor vortices are elucidated and compared in quantitative detail. Simulations in axially periodic systems and in finite systems with stationary rigid ends are compared with experimental spiral data. In a second part of the paper we determine how the above listed properties of the $M=-1$, 0, and 1 vortex structures are changed by an externally imposed axial through flow with Reynolds numbers in the range $-40\leqslant \mathrm{Re}\leqslant 40$. Among other things we investigate when left handed or right handed spirals or toroidally closed vortices are preferred.

DOI: 10.1103/PhysRevE.69.056309 PACS number(s): 47.20.−k, 47.32.−y, 47.54.+r, 47.10.+g

I. INTRODUCTION

Spiral vortices appearing in the annular gap between the concentric rotating cylinders of the Taylor-Couette system [1] are a rather interesting example of the spontaneous formation of a helicoidal structure out of a homogeneous state of a nonlinear forced system when the forcing exceeds a critical threshold. Like the competing toroidally closed Taylor vortices the spiral vortex structures bifurcate out of the unstructured basic state of a circular Couette flow (CCF) that is stable at small rotation rates of the inner cylinder. The spiral pattern breaks the rotational symmetry of the annular gap. It oscillates in time by rotating azimuthally as a whole, thereby propagating axially. The Taylor vortex flow (TVF), on the other hand, is rotationally symmetric and stationary.

The spiral pattern is effectively one dimensional (like the TVF) and stationary when seen from a comoving frame [2]: the spiral fields do not depend on time t, axial coordinate z, and azimuthal angle φ separately but only via the combined phase variable $\phi=kz+M\varphi-\omega(k,M)t$. Here, k and M are the axial and azimuthal wave numbers, respectively, and ω is the frequency. In the $\varphi-z$ plane of an "unrolled" cylindrical surface the lines of constant phase, $\phi=\phi_0$, are straight with slope $-M/k$, as shown in Fig. 1. An azimuthal wave number $M>0$ implies a left handed spiral (L-SPI) while $M<0$ refers to right handed spirals (R-SPI) with our convention of taking k to be positive. The L-SPI and R-SPI being mirror images of each other under the operation $z\rightarrow -z$ are symmetry degenerate flow states. Which of them is realized in a particular experimental or numerical setup depends on the initial conditions.

With the lines of constant phase in the $\varphi-z$ plane being oriented for both spiral types obliquely to the azimuthal "wind" of the basic CCF both spirals are advectively rotated by the latter like rigid objects. Their common angular velocity is $\dot{\varphi}_{\mathrm{SPI}}=\omega(k,M)/M$. This advection enforced rigid-body rotation of the spiral vortices is also reflected by the fact that the axial phase velocities $w_{\mathrm{ph}}=\omega/k=\dot{\varphi}_{\mathrm{SPI}}M/k$ of a L-SPI ($M>0$) and of a R-SPI ($M<0$) are opposite to each other; see Fig. 1. By the same token the rotationally symmetric ($M=0$) structure of toroidally closed Taylor vortices is stationary ($\omega=0$): the lines of constant phases being parallel to the azimuthal CCF the latter cannot advect these vortices. However, an externally imposed axial through-flow can advect Taylor vortices as well as spiral vortices.

The external through-flow breaks the mirror symmetry between the L-SPI and R-SPI. It changes their rotation and propagation dynamics as well as their structural properties and their bifurcation behavior in different ways. This is the topic of our investigation.

In his review [1] Tagg remarked that a systematic investigation of nonaxisymmetric vortex states that appear via primary bifurcations out of the CCF state started remarkably late in the history of the Taylor-Couette problem. Krueger *et*

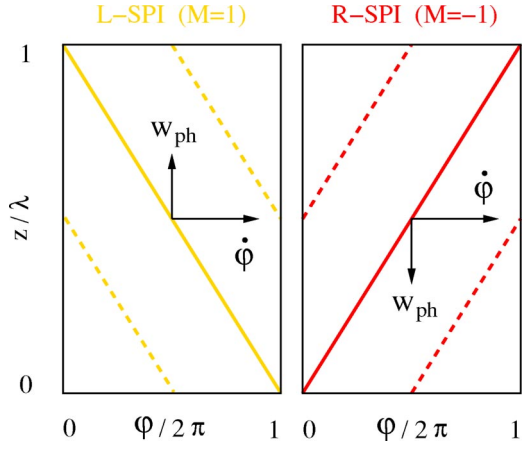

FIG. 1. (Color online) Lines of constant phases, $\phi=$const, for spirals in the $\varphi-z$ plane. Arrows indicate their velocities.

al. [3] in 1966 predicted primary transitions to a nonaxisymmetric rotating-wave flow which then were observed in experiments by Snyder [4], who presented experimental evidence of different types of stable helical flow (referred to as "spirals") a few years earlier. In 1985, an experimental survey was published by Andereck *et al.* [5] which classified a large variety of different flow states, including some spiral types like linear, modulated, interpenetrating, wavy spirals, etc. An extensive numerical linear stability analysis was then performed for a wide range of radius ratios by Langford *et al.* [6]. At this time, Tagg *et al.* [7] experimentally observed a transition from CCF to axially standing and azimuthally traveling waves (ribbons) and found numerically calculated wave speeds to be in agreement with experimental results. Edwards [8] studied the transition from CCF to traveling waves. More recent experiments were done with a system of radius ratio $\eta=0.5$ [9]. Spiral solutions in a relatively narrow gap with axially periodic boundary conditions were obtained numerically with a pseudospectral method using corotating helicoidal coordinates which were adapted to the expected spiral [10].

Various effects of an externally imposed axial through-flow in the Taylor-Couette system have been explored since the early 1930, so that the list of publications cannot be discussed here—see, e.g., Ref. [11] for a partial and far from complete compilation. We mention here in addition a few, more recent papers on selected topics beyond those listed in Ref. [11]: a linear analysis of the competition between shear and centrifugal instability mechanisms [12,13]; linear SPI and TVF fronts and pulses [14]; a weakly nonlinear bifurcation analysis of axially extended spiral, ribbon, and mixed vortex states with homogeneous amplitudes [2,15]; theoretical and numerical investigations of the nonlinear pattern selection in the absolutely unstable regime under downstream evolving intensity envelopes [11]; theoretical and numerical analyses of noise-sustained patterns in the convectively unstable regime [16] (related experiments are listed in Ref. [11]); and analysis of the changes in the noise sensitivity across the convective-absolute stability boundary [17]; and measurements of velocity fields by particle image velocimetry [18].

In this work we explore, in a detailed quantitative investigation, spatiotemporal structures as well as the bifurcation properties of spirals and TVF in a setup with corotating and counter-rotating cylinders of a fixed radius ratio $\eta=0.5$ with and without an externally imposed axial through-flow. Most calculations were done for axially periodic boundary conditions that impose the wave length of the vortex pattern. However, a few simulations of finite systems with rigid, nonrotating lids were also done to compare with experiments and to study the effect of phase propagation suppressing boundaries. The calculations were done with a time dependent finite differences method in the $r-z$ plane combined with a spectral decomposition in φ which by construction yields only the stable flows. However, by selectively suppressing destabilizing modes we also were able to trace out the unstable TVF and SPI solution branches. We do not include in this work results on ribbons [7], i.e., nonlinear combinations of L and R spirals [2] since they were unstable for the parameters investigated here.

In Sec. II we present the notation for describing the Taylor Couette system and we describe our numerical method. In Sec. III we review the spatio-temporal properties of TVF and SPI solutions, and we present results on their bifurcation behavior and flow structure in the absence of through-flow. In particular we provide detailed comparisons of the bifurcation and structural properties of these primary vortex states. Also, comparisons with experiments are presented and discussed. In Sec. IV we elucidate the effect of an external through-flow on structure, dynamics, and bifurcation properties of TVF and SPI methods for counter-rotating cylinders and stationary outer cylinder. Section V contains a summary of the main results.

II. SYSTEM

We report results obtained numerically for a Taylor-Couette system with corotating and counter-rotating cylinders. The ratio $\eta=r_1/r_2$ of the radii r_1 and r_2 of the inner and outer cylinders, respectively, was fixed at the value $\eta=0.5$ for which also experiments have been made recently [9].

A. Theoretical description

We consider the fluid in the annulus between the cylinders to be isothermal and incompressible with a kinematic viscosity ν. The gap width $d=r_2-r_1$ is used as the unit of length and the momentum diffusion time d^2/ν radially across the gap as the time unit so that velocities are reduced by ν/d. To characterize the driving of the system, we use the Reynolds numbers

$$R_1=r_1\Omega_1 d/\nu;\ R_2=r_2\Omega_2 d/\nu. \tag{2.1}$$

These are just the reduced azimuthal velocities of the fluid at the inner and outer cylinders, respectively, where Ω_1 and Ω_2 are the respective angular velocities of the cylinders. The inner one is always rotating counterclockwise, so that Ω_1 and R_1 are positive. We explore positive as well as negative values of R_2 corresponding to co-rotating as well as counter-rotation of the cylinders, respectively. We also elucidate the effect of an externally imposed axial through-flow.

Within the above described scaling, the Navier-Stokes equation (NSE) takes the form

$$\partial_t\mathbf{u}=\boldsymbol{\nabla}^2\mathbf{u}-(\mathbf{u}\cdot\boldsymbol{\nabla})\mathbf{u}-\boldsymbol{\nabla}p. \tag{2.2}$$

Here p denotes the pressure reduced by $\rho\nu^2/d^2$ and ρ is the mass density of the fluid. Using cylindrical coordinates, the velocity field

$$\mathbf{u}=u\mathbf{e}_r+v\mathbf{e}_\varphi+w\mathbf{e}_z \tag{2.3}$$

is decomposed into a radial component u, an azimuthal one v, and an axial one w.

We have solved the resulting equations subject to no slip conditions at the cylinders. In Sec. III D we present simulations of systems with an axial size $\Gamma=12$ and rigid stationary ends bounding the annulus axially in order to compare with experiments [9]. For the main part c.f. Secs. III and IV of this work, however, we imposed, axially periodic boundary conditions at $z=0$ and $z=\Gamma=1.6$. So the axial wavelength of the

TVF and SPI patterns investigated there is $\lambda=1.6$ and the wave number is $k=2\pi/\lambda=3.927$.

B. Numerical method

The calculations were done with a finite difference method in the $r-z$ plane combined with a spectral decomposition in φ. Since we have also been studying finite length cylinders, say, with lids bounding the annulus vertically, here we do not use a spectral decomposition in the axial direction which for axially periodic systems are a generic alternative. The discretization (a FTCS—or forward time, centered space algorithm) has been done on staggered grids in the $r-z$ plane following the procedure of Ref. [19]. It yields simple expressions for the derivatives, it does not require boundary conditions for the pressure, and it avoids difficulties with boundary conditions for more than one velocity field component at the same position. We used homogeneous grids with discretization lengths $\Delta r=\Delta z=0.05$ which have showed to be more accurate than non-homogeneous grids. The time steps were $\Delta t<1/3600$.

Azimuthally all fields $f=u,v,w,p$ were expanded as

$$f(r,\varphi,z,t)=\sum_{m=-m_{\max}}^{m_{\max}} f_m(r,z,t)e^{im\varphi}. \tag{2.4}$$

For the flows investigated here a truncation of the above Fourier expansion at $m_{\max}=8$ was sufficient to properly resolve the anharmonicities in the fields. The system of coupled equations for the amplitudes $f_m(r,z,t)$ of the azimuthal normal modes $-m_{max}\leqslant m\leqslant m_{max}$ is solved with the FTCS algorithm. Pressure and velocity fields are iteratively adjusted to each other with the method of "artificial compressibility" [20]

$$dp^{(n)}=-\beta\,\boldsymbol{\nabla}\cdot\mathbf{u}^{(n)} \quad (0<\beta<1) \tag{2.5}$$

$$p^{(n+1)}=p^{(n)}+dp^{(n)}, \tag{2.6}$$

$$\mathbf{u}^{(n+1)}=\mathbf{u}^{(n)}-\Delta t\,\boldsymbol{\nabla}\,(dp^{(n)}). \tag{2.7}$$

The pressure correction $dp^{(n)}$ in the nth iteration step being proportional to the divergence of $\mathbf{u}^{(n)}$ is used to adapt the velocity field $\mathbf{u}^{(n+1)}$. The iteration loop [Eqs. (2.5)–(2.7)] is executed for each azimuthal Fourier mode separately. It is iterated until $\boldsymbol{\nabla}\cdot\mathbf{u}$ has become sufficiently small for each m mode considered—the magnitude of the total divergence never exceeded 0.02 and typically it was much smaller. After that the next FTCS time step was executed.

For code validation we also compared SPI solutions with experiments [9] and TVF solutions with previous numerical simulations [11] and close to onset with Ginzburg-Landau results [21]. Furthermore, we compared bifurcation thresholds of the nonlinear SPI and TVF solutions with the respective stability boundaries of the linearized NSE [6,14] obtained by a shooting method described in detail in Ref. [14]. As expected from our experience with primary vortex structures in the Taylor-Couette and Rayleigh-Bénard problem lie the FTCS bifurcation thresholds for our discretization typically 1–2 % below the respective linear stability thresholds. This deviation significantly reduces for finer discretizations. We also investigated how the nonlinear solutions change when varying $m_{\max}$ and/or the grid spacing. From these analyses we conservatively conclude that typical SPI frequencies have an error of less than about 0.2 % and that typical velocity field amplitudes can be off by about 3–4 %. Time steps were always well below the von Neumann stability criterion and by more than a factor of 3 below the Courant-Friederichs-Lewy criterion. In order to trace out the unstable parts of bifurcation branches of TVF and SPI solutions we applied different stabilization methods that are described in Sec. III B 1.

III. SPIRAL VORTICES AND TAYLOR VORTICES

In this section we first briefly review spatiotemporal properties of spiral vortices ($M\neq 0$) and Taylor vortices ($M=0$) in the absence of any externally enforced axial through-flow. Here M is the azimuthal wave number of the respective vortex structure. Then we present our results on the bifurcation behavior of $M=0$ and $M=\pm 1$ vortex solutions and on their flow structure.

They both grow out of the basic CCF state, $\mathbf{u}_{\mathrm{CCF}}=v_{\mathrm{CCF}}(r)\mathbf{e}_{\varphi}$, that is rotationally symmetric, axially homogeneous, and time translationally invariant. Here in our system with $\eta=1/2$ the radial profile of its azimuthal velocity reads

$$v_{\mathrm{CCF}}(r)=\frac{2R_2-R_1}{3}r+\frac{4R_1-2R_2}{3}\frac{1}{r}. \tag{3.1}$$

A. Spatiotemporal structure

The spiral vortex structure is periodic in φ, z, and t. It rotates uniformly as a whole like a rigid object in azimuthal direction thereby translating with constant phase velocity in axial direction—the spiral fields $f(r,\varphi,z,t)$ do not depend on φ,z, and t separately but only the phase combination

$$\phi=kz+M\varphi-\omega(k,M)t. \tag{3.2}$$

Here k is the axial wave number that we always take to be positive and $\omega(k,M)$ is the frequency. Thus, with $f(r,\varphi,z,t)=F(r,\phi)$, the spiral pattern is one dimensional. Comparing the Fourier decompositions

$$f(r,\varphi,z,t)=\sum_{m,n} f_{m,n}(r,t)e^{i(m\varphi+nkz)}=\sum_{\nu} F_{\nu}(r)e^{i\nu\phi}=F(r,\phi), \tag{3.3a}$$

one finds that

$$f_{m,n}(r,t)=\delta_{m,nM}e^{-in\omega t}F_n(r). \tag{3.3b}$$

Thus only the mode combinations $m=nM$ appear in a SPI with azimuthal wave number M.

The SPI phase is constant, ϕ_0, on a cylindrical surface, $r=\mathrm{const}$, along lines given by the equation

$$z_0 = -\frac{M}{k}\varphi + \frac{\omega(k,M)}{k}t + \frac{1}{k}\phi_0. \tag{3.4}$$

Thus, on the $\varphi - z$ plane of such an "unrolled" cylindrical surface these lines of constant phase are straight with slope $-M/k$. And an azimuthal wave number $M>0$ implies left handed spirals while $M<0$ refer to right handed spirals with our convention of taking k to be positive. The L-SPI and R-SPI being mirror images of each other under the operation $z \to -z$ are symmetry degenerate flow states. Which of them is realized in a particular experimental or numerical setup depends on the initial conditions.

The lines of constant phase and with it the whole spiral structure rotates in φ with an angular velocity

$$\dot{\varphi}_{\mathrm{SPI}} = \frac{\omega}{M}. \tag{3.5}$$

Its direction strongly depends on the inner cylinder's rotation due to the influence of the CCF. The latter decisively determines the shape of the linear spiral eigenmodes that can grow beyond the stability boundary of the CCF state against perturbations with an azimuthal wave number $M \neq 0$. In the parameter range explored here the spirals rotate in the same direction as the inner cylinder, i.e., in a positive-φ direction, so that $\omega(k,M)/M$ is always positive, i.e., $\omega = \mathrm{sgn}(M)|\omega|$. From this rigid rotation one immediately infers from Eq. (3.2) that the axial phase velocity

$$w_{ph} = \frac{\omega}{k} = \frac{M}{k}\dot{\varphi}_{\mathrm{SPI}} \tag{3.6}$$

of a L-SPI ($M>0$) is positive and that of a R-SPI ($M<0$) is negative.

For the rotationally symmetric ($M=0$) structure of toroidally closed Taylor vortices the lines of constant phases are parallel to e_φ. This $M=0$ pattern is stationary ($\omega=0$). The main reason for this is that the azimuthal flow of the basic CCF state, being precisely parallel to the vortex lines of constant phase, cannot advect them. However, an axial mean flow, being perpendicular to them, can advect them: an externally enforced axial through-flow of strength Re causes a nonzero axial phase velocity of the Taylor vortex pattern that grows linearly with Re, at least when phase pinning effects are absent as for axially periodic boundary conditions.

B. Bifurcation behavior

In the parameter regime considered here the bifurcation thresholds for nonlinear SPI and TVF solutions, i.e., the linear stability boundaries of the CCF state against $M=\pm 1$ and $M=0$ vortex perturbations [6] differ only slightly from each other. For our fixed wave number of $k=3.927$ they intersect at $(R_1^s=95.25, R_2^s=-73.69)$ where these two different vortex modes are "bicritical" in the sense that their growth rates are simultaneously zero. The stability boundaries were obtained with a shooting method from the linearized NSE. The nonlinear SPI and TVF solutions, that were determined with the numerical method described in Sec. II B give bifurcation thresholds that differ as a result of the FTCS discretization errors by at most 2 % from the linear stability analysis. However, this difference can grow with externally applied through-flow up to, say, 5 % at $\mathrm{Re} \simeq 40$ (cf. Sec. IV) when the discretization is not refined.

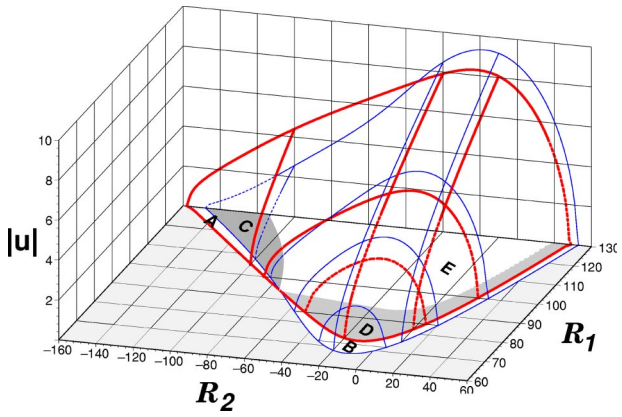

FIG. 2. (Color online) Order parameter bifurcation surfaces of TVFs (thin lines) and SPIs (thick lines) over the R_1-R_2 plane. Shown are primary Fourier amplitudes, $|u_{m,n}|$, of the radial flow intensity at midgap, $r=r_1+0.5$, with axial mode index $n=\pm 1$. The azimuthal one is $m=0$ for TVFs and $m=\pm 1$ for SPIs, respectively. In each case full (dashed) lines denote stable (unstable) solutions.

Region	A	B	C	D	E
TVF	-	stable	unstable	stable	stable
SPI	stable	-	stable	unstable	stable

1. Radial flow amplitudes of TVF and SPI

The bifurcation of both, TVF and SPI solutions is forward as shown by the bifurcation surface over the R_1-R_2 plane of Fig. 2. There the respective vortex solution is characterized by the primary Fourier amplitude, $|u_{m,n}|$, of the radial flow intensity at midgap, $r=r_1+0.5$, taken as order parameter with m denoting the azimuthal mode index and n referring to the axial one, respectively. Thus, Fig. 2 shows $|u_{0,1}|$ for the TVF solution by thin lines, and $|u_{1,1}|=|u_{-1,1}|$ for the two symmetry degenerate $M=\pm 1$ solutions by thick lines, respectively. In each case stable (unstable) solutions are represented by full (dashed) lines. The different stability regions labeled A–E are explained in the caption of Fig. 2.

The stability of the vortex states refers to our system with fixed axial periodicity length. Thus, e.g., Eckhaus or Benjamin-Feir instabilities [22] that can destabilize periodic patterns in infinite and large systems do not occur here. Furthermore, our periodic boundary conditions allowing free phase propagation enhance the existence range as well as the stability range of SPI solutions in comparison with, say, Ekman vortex generating stationary lids that axially close the annulus in an experimental setup. The latter suppress phase propagation in their vicinity so that phase generating and phase destroying defects near opposite boundaries are necessary for the realization of spirals in the bulk of such systems.

In our setup TVF is for $R_2 > R_2^s$ stable close to onset. And it remains so at least up to the largest value of $R_1=130$

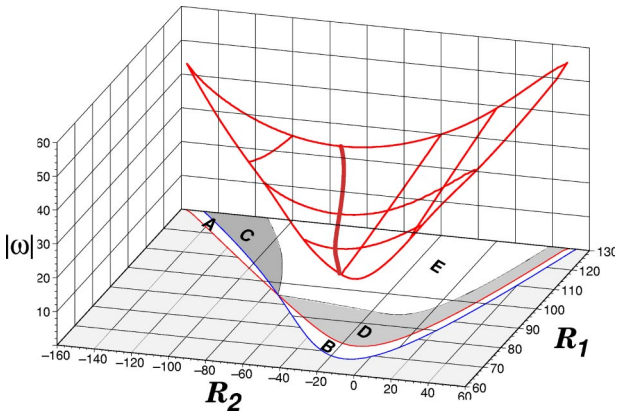

FIG. 3. (Color online) Bifurcation diagram of $M=\pm 1$ spiral frequencies ω over the R_1-R_2 plane. The thick line locates the minima. The different stability regions A–E of TVF and of SPI solutions (cf. caption of Fig. 2) in the R_1-R_2 plane are included for a better comparison with Fig. 2.

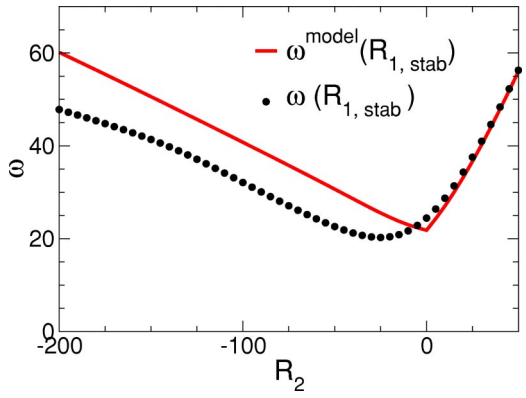

FIG. 4. (Color online) Linear frequency $\omega(R_{1,\mathrm{stab}})$ of the $M=1$ spiral at onset, $R_{1,\mathrm{stab}}(R_2)$, in comparison with the frequency $\omega^{\mathrm{model}}(R_{1,\mathrm{stab}})$ [Eq. (3.7)] resulting from a rigid-body rotation model.

shown in Fig. 2—for larger R_1 the TVF eventually undergoes an oscillatory instability. For more negative $R_2<R_2^s$ the TVF is unstable at onset (region C in Fig. 2) but becomes stable at larger R_1 in region E. The unstable TVF solution branch in region C was obtained by suppressing any $m\neq 0$ modes in the field representation (2.4), i.e., by allowing only rotationally symmetric solutions. Lifting this mode restriction infinitesimal $m\neq 0$ perturbations drive the system in the parameter region C of Fig. 2 away from the unstable TVF solution into a stable SPI state.

Spirals, on the other hand, are for $R_2<R_2^s$ stable close to onset and remain so at least up to the largest value of $R_1=130$ shown in Fig. 2 while for $R_2>R_2^s$ they are unstable at onset (region D in Fig. 2). But then they become stable at larger R_1 in region E. The unstable SPI solution branch in region D was obtained by suppressing $m=0$ contributions to the radial velocity field u at mid gap location. This stabilized the SPI solution against the growth of the TVF. Lifting this restriction of the available mode space the unstable SPI solutions in region D decay into stable Taylor vortices.

In the relatively large region E both, SPI as well as TVF solutions coexist bistably and the final vortex structure to be found here depends on the initial conditions and the driving history of R_1 and R_2. Note in particular that for our periodic boundary conditions the region E with stable spirals extends to positive R_2, i.e., to a situation with corotating cylinders.

2. SPI freqencies

In Fig. 3 the spiral frequencies ω are plotted over the same control parameter range as the radial flow amplitudes in Fig. 2. Also here we include—for the sake of comparison with Fig. 2—the identification of the different stability regions of TVF and SPI solution by the symbols A–E explained in the caption of Fig. 2. At onset ω agrees within the numerical accuracy of our nonlinear code with the eigenvalue resulting from the linear stability analysis of the CCF state.

The nonlinear SPI frequencies further away from onset vary smoothly: the bifurcation surface of ω in Fig. 3 has the shape of a cloth that hangs down from a frame given by the linear onset spiral frequencies $\omega(R_{1,\mathrm{stab}})$ at the stability threshold $R_{1,\mathrm{stab}}(R_2)$ of the CCF. The location of minimal ω on the bifurcation surface is shown by a thick line in Fig. 3. Thus, the nonlinear SPI frequencies are typically smaller than the linear ones but do not deviate substantially from them.

Since the linear onset frequencies show a characteristic variation along the bifurcation threshold, $R_{1,\mathrm{stab}}(R_2)$, that dictates the form of the whole ω bifurcation surface, we discuss them in some detail. They, furthermore allow for a simple, yet semiquantitive explanation of the phenomenon of rigid body rotation of spirals in terms of a passive advection dynamics of $M=\pm 1$ vortex perturbations, $e^{i\phi}$, with lines of constant phase, $\phi=kz+M\varphi-\omega t$, that are oriented obliquely to the "wind" of the basic azimuthal CCF. To that end, in Fig. 4 we compare the onset spiral frequency $\omega(R_{1,\mathrm{stab}})$ at the stability threshold $R_{1,\mathrm{stab}}(R_2)$ of the CCF with the "model" frequency $\omega^{\mathrm{model}}(R_{1,\mathrm{stab}})$ which is also evaluated at the stability threshold $R_{1,\mathrm{stab}}(R_2)$. Here

$$\omega^{\mathrm{model}}=\langle\omega_{\mathrm{CCF}}(r)\rangle=\frac{2}{r_0^2-r_1^2}\int_{r_1}^{r_0}\omega_{\mathrm{CCF}}(r)r\,dr \qquad (3.7)$$

is the mean of the rotation rate of the CCF, $\omega_{\mathrm{CCF}}=v_{\mathrm{CCF}}/r$. For $R_2<0$ the averaging is done over the radial domain between inner cylinder, r_1, and the first zero, r_0, of $v_{\mathrm{CCF}}(r)$ [Eq. (3.1)]. Thus, at the stability threshold $R_{1,\mathrm{stab}}(R_2)$ one has

$$r_0^2=\frac{2R_2-4R_{1,\mathrm{stab}}}{2R_2-R_{1,\mathrm{stab}}}, \qquad (3.8)$$

when $R_2<0$ However, when $R_2\geqslant 0$, i.e., when v_{CCF} remains positive throughout the gap r_0 is replaced by r_2. The restriction of the radial average to the range between r_1 and r_0 is motivated by an argument of largely hand-waving nature: the linear eigenfunctions for marginally stable SPI modes are somewhat centered to this range where the growth of vortex perturbations is supported.

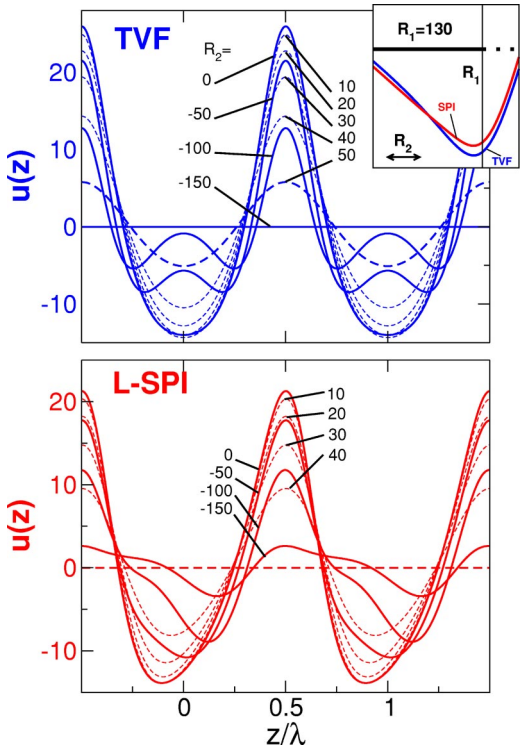

FIG. 5. (Color online) Axial profiles of the radial velocity $u(z)$ at the midgap position for $R_1=130$ and various R_2 (along the thick horizontal line in the inset) covering the whole interval between the bifurcation thresholds marked TVF and SPI, respectively, in the inset; see also Fig. 2. Full (dashed) lines refer to negative (positive) R_2. In each case the maximal radial outflow is chosen to lie at $z=0.5\lambda$. For better visibility two axial periods of the vortex profiles are shown. The $M=1$ L-SPIs are propagating in positive z direction. Parameters are $\eta=0.5$ and $k=3.927$.

Figure 4 shows that the onset spiral frequency $\omega(R_{1,\mathrm{stab}})$ agrees perfectly well with the mean CCF rotation frequency [Eq. (3.7)] when $R_2>0$. For $R_2<0$ the model ansatz (3.7) for the global spiral rotation rate overestimates slightly the spiral frequency since Eq. (3.7) does not contain contributions from negative CCF rotation rates between r_0 and r_2. In fact, if one extends in an ad hoc way the averaging domain slightly beyond r_0 then the agreement improves significantly. Thus, the onset spiral frequency $\omega(R_{1,\mathrm{stab}})$, i.e., the frequency eigenvalue can be seen as the mean rotation rate of the CCF—albeit weighted appropriately by the critical eigenfunctions.

C. Flow structure of the TVF and SPI

In this section we elucidate the flow structure of spiral vortices in comparison with Taylor vortices. To that end we consider the radial velocity field. In Fig. 5 we show the axial profiles of $u(z)$ at a midgap position for $R_1=130$ being fixed and various R_2 that cover the whole interval between the bifurcation thresholds (cf. Fig. 2 and the inset of Fig. 5). Full (dashed) lines refer to negative (positive) R_2. In each case the axial position of maximal radial outflow is chosen to lie at $z=0.5\lambda$. For the sake of better visibility two axial periods of the vortex profiles are shown.

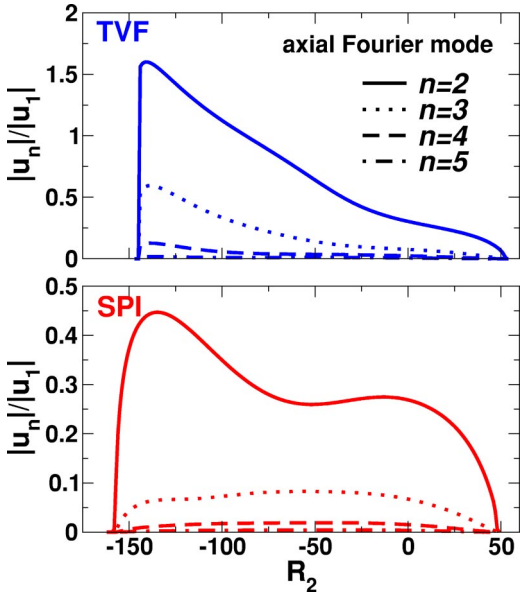

FIG. 6. (Color online) Anharmonicity of the TVF and SPI. The ratios $|u_n/u_1|$ of the axial Fourier modes of the profiles of $u(z)$ shown in Fig. 5 are displayed here as functions of R_2 for fixed $R_1=130$. The bifurcation thresholds are located at the zeros. Parameters are $\eta=0.5$ and $k=3.927$.

1. Anharmonicity: TVF versus SPI

Typically SPIs are less anharmonic than TVFs. Also the profiles of both are less anharmonic for positive R_2 than for negative R_2 and the degree of anharmonicity increases when R_2 becomes more negative. For the mirror symmetric TVF this anharmonicity growth comes from a widening (narrowing) of the axial range Δ_{in} (Δ_{out}) of radial inflow over which $u<0$ ($u>0$) and the corresponding decrease (increase) of the inflow (outflow) velocity. For the L-SPI that propagate in Fig. 5 in the positive z direction the anharmonicity grows mainly by flattening (steepening) the wave profiles ahead of (behind) the crests. However, $\Delta_{\mathrm{in}}/\Delta_{\mathrm{out}}$ increases also for a SPI albeit less than for a TVF.

The variation of the anharmonicity of the vortex profiles can be read off more quantitatively from the results of an axial Fourier analysis. To that end, in Fig. 6 we show the ratios $|u_n/u_1|$ of the nth and first axial Fourier modes of the profiles of Fig. 5 as a function of R_2 for fixed R_1. With growing distances from the bifurcation thresholds at positive and negative R_2 the anharmonicity grows for the TVF as well as for the SPI. It does so most precipitously near the thresholds at negative R_2 of about -150 in Fig. 6.

At negative R_2 the anharmonicity of the TVF can be for rapidly counter-rotating cylinders already close to threshold so large that $|u_2/u_1|>1$. This property reflects the fact that for sufficiently negative R_2 Taylor vortices are effectively smaller in size than the gap width. There are two main reasons for this size reduction which are both connected to the tendency of vortices to have circular shapes: (i) the axial periodicity length $\lambda=1.6$ reduces the *axial* vortex size relative to the gap and, more importantly, (ii) the TVF intensity is *radially* restricted not to extend significantly beyond the zero of the CCF at r_0 since according to the Rayleigh crite-

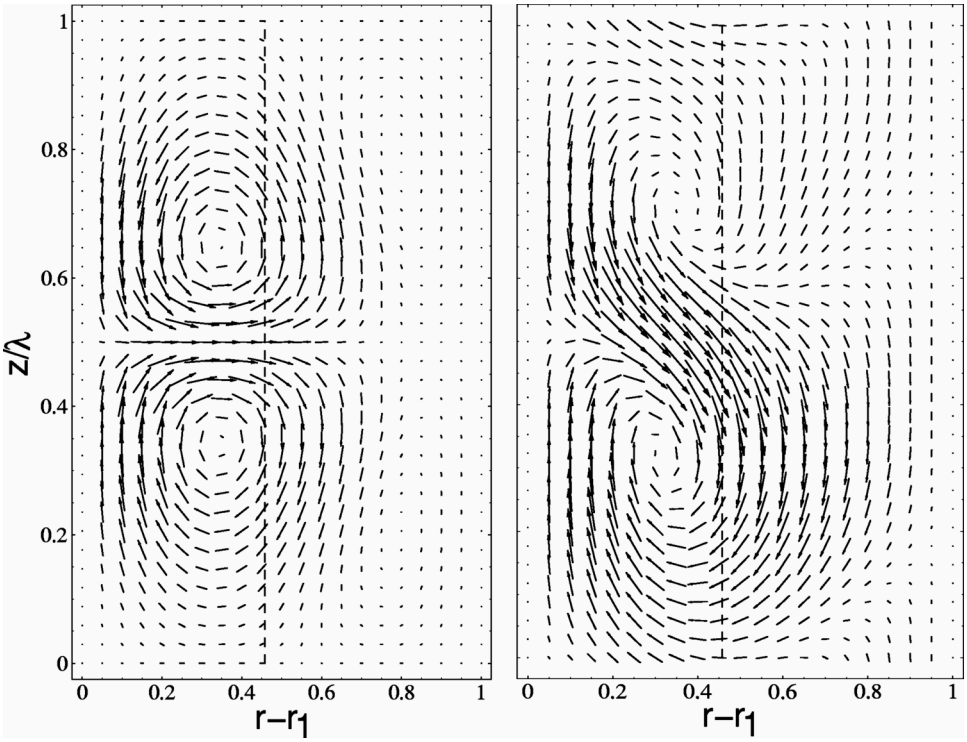

FIG. 7. Velocity field (u,w) of the TVF (left) and L-SPI (right) in an $r-z$ plane. Vertical lines locate the zero of the azimuthal CCF flow $v_{CCF}(r)$. Parameters are $\eta=0.5$, $k=3.927$, $R_1=120$, and $R_2=-100$.

rion $m=0$ radial momentum transport is suppressed by opposite pressure gradients for $r>r_0$ where the CCF stratification of the squared angular momentum density is stable. With R_2 becoming more negative r_0 moves inwards and the radial size of Taylor vortices reduce.

However, the $m=0$ Rayleigh criterion does not apply to the SPI. Their $m\neq 0$ radial momentum transport extends further beyond r_0. Therefore SPI vortices fill out the whole gap more than Taylor vortices, (cf. Fig. 7), and consequently they are less anharmonic.

2. Mirror symmetry breaking of the SPI

The TVF shows axial mirror symmetry around the position of maximal radial outflow, $z=0.5\lambda$, in Fig. 5. In order to measure the degree to which this symmetry is broken in the SPI we have used the asymmetry parameter

$$P=\frac{\int |u(z')-u(-z')|dz'}{\int |u(z')+u(-z')|dz'}, \tag{3.9}$$

evaluated at midgap with $z'=0$ locating the largest radial SPI outflow at this r value. In this way we found, e.g., for the spirals of Fig. 5, that the smallest $P\simeq 0.2$ occurs for spirals with the smallest frequency $\omega_{\min}\simeq 23.4$ at $R_2\simeq -74$. Increasing R_2 from this value all the way toward the upper SPI bifurcation threshold at $R_2\simeq 48$ the frequency increases but P remains roughly unchanged at about 0.2. On the other hand, when decreasing R_2 from -74 the asymmetry parameter increases with increasing ω up to $P\simeq 1$ close to the lower SPI bifurcation threshold $R_2\simeq -158$. Thus, fast propagating spirals at large negative R_2 show the largest mirror symmetry breaking.

D. Comparison with experimental results

In order to check our numerical results we made a few comparisons with experiments. For example, in Fig. 8 we show the axial profile of the radial flow $u(z)$ of a L-SPI at $r_1+0.4$. Symbols denote laser-Doppler velocimetry measurements [9] and the full line a numerical simulation, both done in a setup height $\Gamma=12$ with rigid, nonrotating lids at both ends of the annulus. In each case the spirals were monitored at mid-height of the cylinders where they had the common wavelength $\lambda\simeq 1.76$. Since absolute experimental velocities were not available we have scaled the experimental maximum in Fig. 8 to that of our simulation (full line). Without knowledge of the experimental error-bars we consider the agreement between symbols and full line to be satisfactory.

The dashed line shows a numerical profile obtained for axially periodic boundary conditions imposing the wavelength $\lambda=1.6$. It differs slightly from the SPI profile (full line) in the bulk part of the $\Gamma=12$ system with rigid ends. The difference is presumably related to the fact that the axial flow, and in particular the mean-flow w_0 (4.4), is different in these two cases as discussed in Sec. IV A 2.

In Fig. 9 we compare the frequency variation of experimental and numerical L-SPI with R_1. Symbols and the full line come from laser-Doppler velocimetry measurements [9] and numerical simulations, respectively, of the aforementioned Taylor-Couette setup ($\eta=0.5$) of height $\Gamma=12$ with

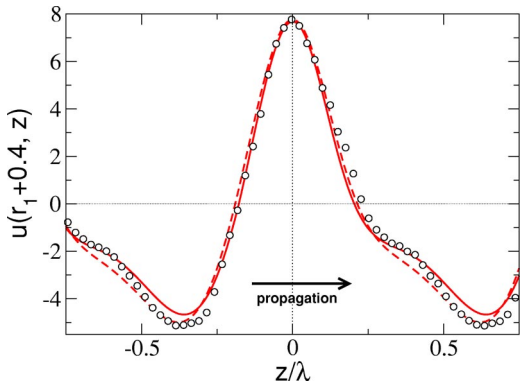

FIG. 8. (Color online) Comparison of experimental and numerical axial profiles of the radial velocity $u(r_1+0.4,z)$ of a L-SPI. For better visibility more than one period is shown. Symbols and the full line denote laser-Doppler velocimetry measurements [9] and numerical simulations, respectively, of a Taylor-Couette setup of height $\Gamma=12$ with rigid, nonrotating lids at both ends. Both refer to the bulk region at mid height with a common local wavelength of $\lambda\simeq 1.76$. There the experimental maximum of u is scaled to our simulation result. The dashed line refers to a simulation done with axially periodic conditions imposing a wavelength of $\lambda=1.6$. Common parameters are $\eta=0.5$ and $R_1=111$, with $R_2=-95$ for the experiments and $R_2=-96$ for the simulations.

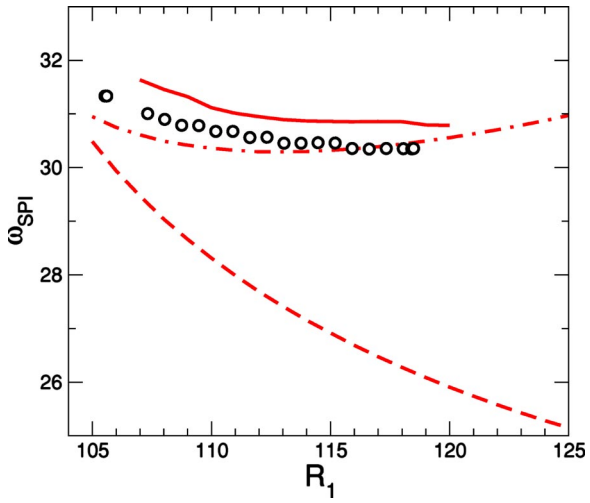

FIG. 9. (Color online) Comparison of the frequency variation of experimental and numerical L-SPIs with R_1. Symbols and the full line come from laser-Doppler velocimetry measurements [9] and numerical simulations, respectively, of a Taylor-Couette setup ($\eta=0.5$) of height $\Gamma=12$ with rigid, nonrotating lids at both ends that enforce the net mean axial flow $\langle w\rangle$ [Eq. (4.3)] to vanish. The dashed line refers to a simulation done with axially periodic conditions ($\lambda=1.6$). They allow for a finite Reynolds-stress-sustained $\langle w\rangle$ that is negative for our parameters. Upon subtracting this Galilean contribution $\langle w\rangle k$ from the oscillation frequency under periodic boundary conditions (dashed line) one obtains the dash-dotted line that lies close to the SPI frequencies with rigid end conditions. Common parameters are $R_2=-96$; however, $R_2=-100$ for the full line.

rigid, non-rotating lids at both ends. Note that not only the frequency values of these experimental and numerical SPI states agree reasonably well with each other but also their existence range in R_1. Its lower end marks the oscillatory onset. At the upper end in R_1 these SPIs lose their stability to the TVF—in experiments as well as in the simulations.

However, under axially periodic boundary conditions the existence range of stable SPIs extends to significantly larger values of R_1 lying outside of the plot range of Fig. 9. The dashed line in Fig. 9 refers to simulations done with axially periodic conditions ($\lambda=1.6$) that allow for a free propagation of phase. In addition, they allow the Reynolds-stress-sustained mean axial flow w_0 [Eq. (4.4)] to have a finite *net* part $\langle w\rangle$ [Eq. (4.3)] that is negative for our parameters—cf. Sec. IV A 2. In order to compare with the SPI frequencies for rigid end conditions we subtract from the oscillation frequencies under periodic boundary conditions (dashed line) the pure Galilean contribution $\langle w\rangle k$ and obtain the dash-dotted line. Note how close the latter lies to the SPI frequencies in the system with rigid end conditions. Thus, we find that the SPI frequency differences [15] for the two different end boundary conditions are mostly due to whether the Galilean contribution $\langle w\rangle k$ is suppressed or not.

IV. EXTERNAL THROUGH-FLOW

Here we discuss the influence of an externally imposed axial through-flow on spiral and Taylor vortices. Since the effect of an axial through-flow on a TVF has been investigated for $R_2=0$ in several works, we focus our investigation on SPI vortices.

The through-flow is enforced by adding in the NSE for the axial velocity component a constant pressure gradient of size $\partial_z p_{\mathrm{APF}}$ throughout the annulus. In the absence of any vortex flow, i.e., for sub-critical control parameters this pressure gradient, $\partial_z p_{\mathrm{APF}}$, drives an annular Poiseuille flow (APF) with a radial profile of the axial through-flow velocity given by

$$w_{\mathrm{APF}}(r)=\frac{\partial_z p_{\mathrm{APF}}}{4}\left[r^2+\frac{1+\eta}{(1-\eta)\ln\eta}\ln r+\frac{(1+\eta)\ln(1-\eta)}{(1-\eta)\ln\eta}-\frac{1}{(1-\eta)^2}\right]. \tag{4.1}$$

We checked that our numerical code reproduces this analytical solution (4.1) of the NSE. We use its mean to define the through-flow Reynolds number by

$$\langle w_{\mathrm{APF}}(r)\rangle=\mathrm{Re}=-\frac{\partial_z p_{\mathrm{APF}}}{8}\frac{1-\eta^2+(1+\eta^2)\ln\eta}{(1-\eta)^2\ln\eta}. \tag{4.2}$$

Hence positive (negative) Re implies an axial flow, $w_{\mathrm{APF}}(r)$, in the positive (negative) z direction. The last equality in Eq. (4.2) establishes the relation between the externally applied additional axial pressure gradient and the through-flow Reynolds number Re.

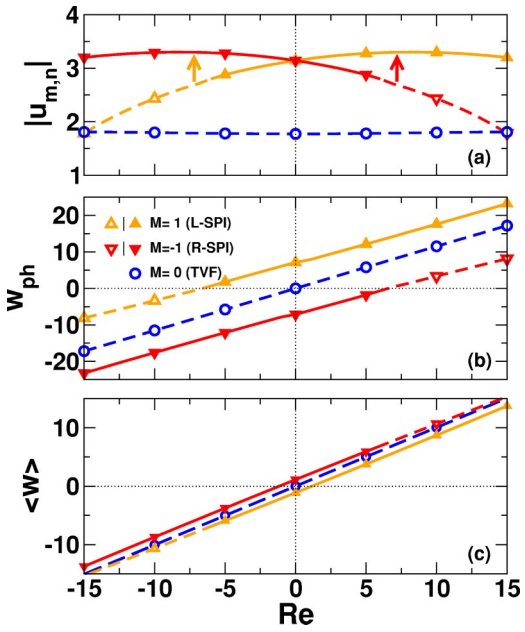

FIG. 10. (Color online) Influence of an external through-flow on vortex structures. (a) Primary Fourier amplitudes of the radial flow field at midgap for the $M=1$ L-SPI ($u_{1,1}$), the $M=-1$ R-SPI ($u_{-1,1}$), and for the TVF ($u_{0,1}$). (b) Axial phase velocity $w_{ph}=\omega/k$. (c) Net mean axial flow $\langle w\rangle$ [Eq. (4.3)]. Full (dashed) lines with filled (open) symbols refer to stable (unstable) states. Arrows indicate transitions after loss of stability, see text for details. The TVF is unstable in the Re range shown here for our parameters $R_1=120$, $R_2=-100$, $\eta=0.5$, and $k=3.927$.

A. Counter-rotating cylinders

Figure 10 shows how the through-flow influences the L-SPI, R-SPI, and TVF at the fixed characteristic driving combination $R_1=120$ and $R_2=-100$ that is located in Figs. 2 and 3 in region C close to the border to region E. For this parameter combination the TVF is unstable when $\mathrm{Re}=0$ and it remains unstable in the Re range shown in Fig. 10. This is of relevance for the through-flow induced transitions between the L-SPI and R-SPI (cf. further below).

1. Bifurcation behavior

In Fig. 10(a) we present primary Fourier amplitudes, $|u_{m,n}|$ of the radial flow intensity at midgap versus Re. These are $|u_{1,1}|$ for the $M=1$ L-SPI, $|u_{-1,1}|$ for the $M=-1$ R-SPI, and $|u_{0,1}|$ for the TVF. Figure 10(b) shows their axial phase velocity, $w_{ph}=\omega/k$, and Fig. 10(c) shows the *net* mean axial flow

$$\langle w\rangle=\frac{1}{\pi(r_2^2-r_1^2)}\int_0^{2\pi}\int_{r_1}^{r_2} w(r,\varphi,z,t)rdr\,d\varphi. \qquad (4.3)$$

For $\mathrm{Re}=0$ the two spirals are mirror images of each other: their radial velocities are the same and all respective axial velocities have the same magnitude but opposite direction. Note that the SPI Reynolds stresses drive an axial flow to be discussed further below. Its net mean, $\langle w\rangle$ [Eq. (4.3)], is directed opposite to the phase velocity, w_{ph}, of the respective spiral when $\mathrm{Re}=0$. Note, however, the difference in size between $|w_{ph}|\simeq 7.1$ and $|\langle w\rangle|\simeq 1.1$ [23].

A finite through-flow breaks the mirror symmetry between the $M=1$ L-SPI and the $M=-1$ R-SPI. Their radial flow amplitudes evolve with through-flow as shown in Fig. 10(a). We performed also a linear stability analysis of the combined CCF-APF state. It shows that for our control parameters $R_1=120$ and $R_2=-100$, the amplitudes of the $M=\pm 1$ SPI solutions go to zero at the bifurcation threshold values of $\mathrm{Re}=\mp 19.07$ and ± 50.95. The numerical solutions of the full nonlinear NSE showed, in addition, that the L-SPI (R-SPI) is unstable near the first threshold, $\mathrm{Re}\simeq -19$ ($\mathrm{Re}\simeq 19$), and that it is stable near the second one, $\mathrm{Re}\simeq 50$ ($\mathrm{Re}\simeq -50$).

For small through-flow—say, for $-6\lesssim \mathrm{Re}\lesssim 6$ in Fig. 10—the two spiral solutions coexist bistably; their particular realization depending on initial conditions. However, with increasing $|\mathrm{Re}|$ that spiral suffers a through-flow enforced loss of stability for which the phase velocity changes sign. This happens roughly when the through-flow has become sufficiently strong to revert an originally adverse axial phase propagation. For example, the $M=-1$ R-SPI of Fig. 10 propagates for small $\mathrm{Re}\lesssim 6.6$ axially downwards (i.e., opposite to the externally imposed through-flow) as for $\mathrm{Re}=0$, then become stationary, and finally propagates upwards in through-flow direction for $\mathrm{Re}\gtrsim 6.6$. Similarly, by symmetry, the $M=1$ L-SPI propagates in a small negative through-flow upwards against the through-flow for $\mathrm{Re}\gtrsim -6.6$ and downwards, i.e., in through-flow direction for $\mathrm{Re}\lesssim -6.6$.

The direction of the imposed through-flow is the preferred one for stable phase propagation: A spiral that has started at small $|\mathrm{Re}|$ to move against the wind dies out—or, more precisely, becomes unstable—when the wind becomes sufficiently strong to turn it back. Only that SPI is stable at large $|\mathrm{Re}|\gtrsim 7.2$ in Fig. 10 that keeps propagating into the preferred direction of the through-flow. The other one is unstable at large $|\mathrm{Re}|$.

The through-flow enforced loss of stability of one SPI state and the transition to the remaining stable one is indicated schematically in Fig. 10(a) by vertical arrows. However, we should like to stress that the transition is somewhat complex extending over the through-flow interval $6\lesssim|\mathrm{Re}|\lesssim 7.2$ the center of which locates the zero of w_{ph} at $|\mathrm{Re}|\simeq 6.6$. In this interval there are stable, mixed states with finite L- and R-SPI modes. Their amplitudes seem to vary largely continuously with Re (with possibly some saddle-node discontinuity) between the pure (SPI) solutions: the amplitude of the spiral that loses the stability competition decreases with growing $|\mathrm{Re}|$ towards zero while the amplitude of the winning one increases from zero to the pure monostable final SPI state.

Note that since the TVF is unstable for the parameters of Fig. 10 it does not offer an alternative transition to a final $M=0$ state as for the parameters of Sec. IV B. There, for $R_2=0$, the through-flow induces a transition to a stable (TVF) rather than to the stably coexisting SPI with preferred propagation direction. Only when the TVF is eliminated there does the transition occur to the then monostable spiral—for details see Sec. IV B.

We also made a few calculations in a regime where the TVF stably coexists with the SPI for counter-rotating

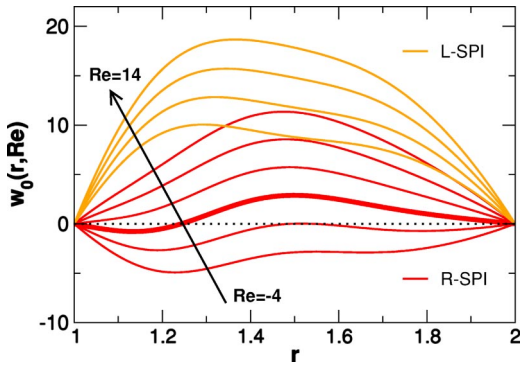

FIG. 11. (Color online) Radial profiles of the axial mean flow $w_0(r)$ [Eq. (4.4)] of spirals shown in Fig. 10 for axial Reynolds numbers $-4 \leqslant \mathrm{Re} \leqslant 14$ increasing in steps of 2. The thick line refers to $\mathrm{Re}=0$. The transition from R- to L-SPI occurs around $\mathrm{Re} \simeq 7$; cf. the text. Parameters are $R_1=120$, $R_2=-100$, $\eta=0.5$, and $k=3.927$.

cylinders. Also then the through-flow preferably induces a transition to a stable TVF state rather than to a stable SPI state. Thus, when the through-flow destabilizes, e.g., the $M=-1$ R-SPI, then typically the $M=0$ TVF modes grow rather than the $M=1$ L-SPI modes.

2. Axial velocities w_{ph}, w_0, and $\langle w \rangle$

In the through-flow range shown in Fig. 10 the phase velocity w_{ph} and the net mean flow $\langle w \rangle$ vary roughly linearly with *Re*. The slopes $\partial w_{ph}/\partial \mathrm{Re}$ and $\partial \langle w \rangle / \partial \mathrm{Re}$ for the SPI well as for the TVF are roughly 1.

While the phase of the $M=\pm 1$SPI reverts its propagation direction at $\mathrm{Re} \simeq \mp 6.6$ the net mean flow changes sign already at $\mathrm{Re} \simeq \pm 1.2$. The reversal of the latter does not seem to have any consequence. But the through-flow enforced reversal of the phase velocity seems to be responsible for the destabilization of the (SPI) that propagate at small $|\mathrm{Re}|$ against the wind, i.e., in the "wrong" direction.

In Fig. 11 we show how the radial profiles of the mean axial flow,

$$w_0(r) = \frac{1}{2\pi} \int_0^{2\pi} w(r,\varphi,z,t) d\varphi, \tag{4.4}$$

of spirals shown in Fig. 10 evolve with the through-flow in the range $-4 \leqslant \mathrm{Re} \leqslant 14$. We checked that w_0 is independent of z and t and that our spirals propagating in the externally imposed axial pressure gradient still have the SPI symmetry, i.e., the flow fields depend on z, φ, and t only via the phase combination ϕ [Eq. (3.2)] with an oscillation frequency ω that is modified by the through-flow. Then one finds from the NSE for the $m=0$ azimuthal mode of the axial velocity field,

$$\left(\partial_r + \frac{1}{r}\right) \partial_r w_0 = \left(\partial_r + \frac{1}{r}\right) (uw)_0 + \partial_z p_0, \tag{4.5}$$

that the SPI mean flow can be driven by Reynolds stresses and/or by mean axial pressure gradients. For $\mathrm{Re}=0$ the pressure is enforced to be axially periodic, hence $\partial_z p_0(\mathrm{Re}=0)=0$. So in that case the mean axial flow is driven solely by the nonlinear Reynolds stresses. They are rather large. For example for the R-SPI propagating at $\mathrm{Re}=0$ in the negative-z direction with phase velocity $w_{\mathrm{ph}} \simeq -7.1$ the maximum of $w_0(r)$ is about 3, i.e., directed opposite to the phase propagation and almost half as large in magnitude as w_{ph}. The *net* mean flow $\langle w \rangle$ [Eq. (4.3)] is for this case still about 1.1 and also opposite to w_{ph}.

As an aside we mention that rigid axial end conditions enforce $\langle w \rangle = 0$ throughout the annulus. They generate an adverse axial pressure gradient that compensates for the Reynolds stresses [25] so that w_0 is practically zero in the bulk part where SPIs are realized. Only in the Ekman region w_0 becomes finite showing TVF behavior there.

For the R-SPI of Fig. 11 propagating at $\mathrm{Re}>0$ opposite to the external through-flow the maximal mean flow is located roughly at midgap. However, for the SPI propagating in the direction of the external through-flow, i.e., the R-SPI for $\mathrm{Re}<0$ and the L-SPI for $\mathrm{Re}>0$, the extremum of $w_0(r)$ is shifted towards the inner cylinder. The mean flow profiles of the spirals of Fig. 11 are given within about 5 % by the superposition

$$w_0(r;\mathrm{Re}) \simeq w_0(r;\mathrm{Re}=0) + w_{\mathrm{APF}}(r;\mathrm{Re}) \tag{4.6}$$

of the pure, Reynolds stress generated flow $w_0(\mathrm{Re}=0)$ of the respective SPI plus the pure, pressure gradient enforced APF flow $w_{\mathrm{APF}}(\mathrm{Re})$ [Eq. (4.1)]. This holds for the L-SPI as well as for the R-SPI irrespective of whether they propagate in the direction of the through-flow or against it.

3. Spiral profiles

The through-flow changes the structure of the SPI. This is documented in Figs. 12 and 13. The arrows in Fig. 12 representing the u,w vector field of the L-SPI in the $r-z$ plane show the effect of imposing an axial through-flow that increases from $\mathrm{Re}=-5$ (a) to $\mathrm{Re}=10$ (d) in steps of five. Note, however, that the externally imposed axial pressure gradient does not just add $w_{\mathrm{APF}}(r)$ to the axial velocity field w. It also modifies all vector field components of the SPI. The axial profile of the radial flow $u(z)$ for example is changed by the through-flow as shown in Fig. 13 for increasing Re. Here the axial asymmetry of the upwards propagating L-SPI is reduced by steepening up the leading part of $u(z)$ ahead of the wave crests. This reduction of the mirror-asymmetry of the radial flow of the L-SPI grows somewhat linearly with increasing Re. As an aside we mention that, on the other hand, the TVF profiles of $u(z)$ become with increasing Re more and more asymmetric—the mirror asymmetry parameter P [Eq. (3.9)] increases for the TVF linearly with Re.

B. Nonrotating outer cylinder

We have also investigated the influence of an externally imposed axial through-flow on TVFs and SPIs for stationary outer cylinder, $R_2=0$.

1. Bifurcation behavior

In Fig. 14 we show the bifurcation behavior of TVFs and SPIs as a function of through-flow Reynolds number Re for

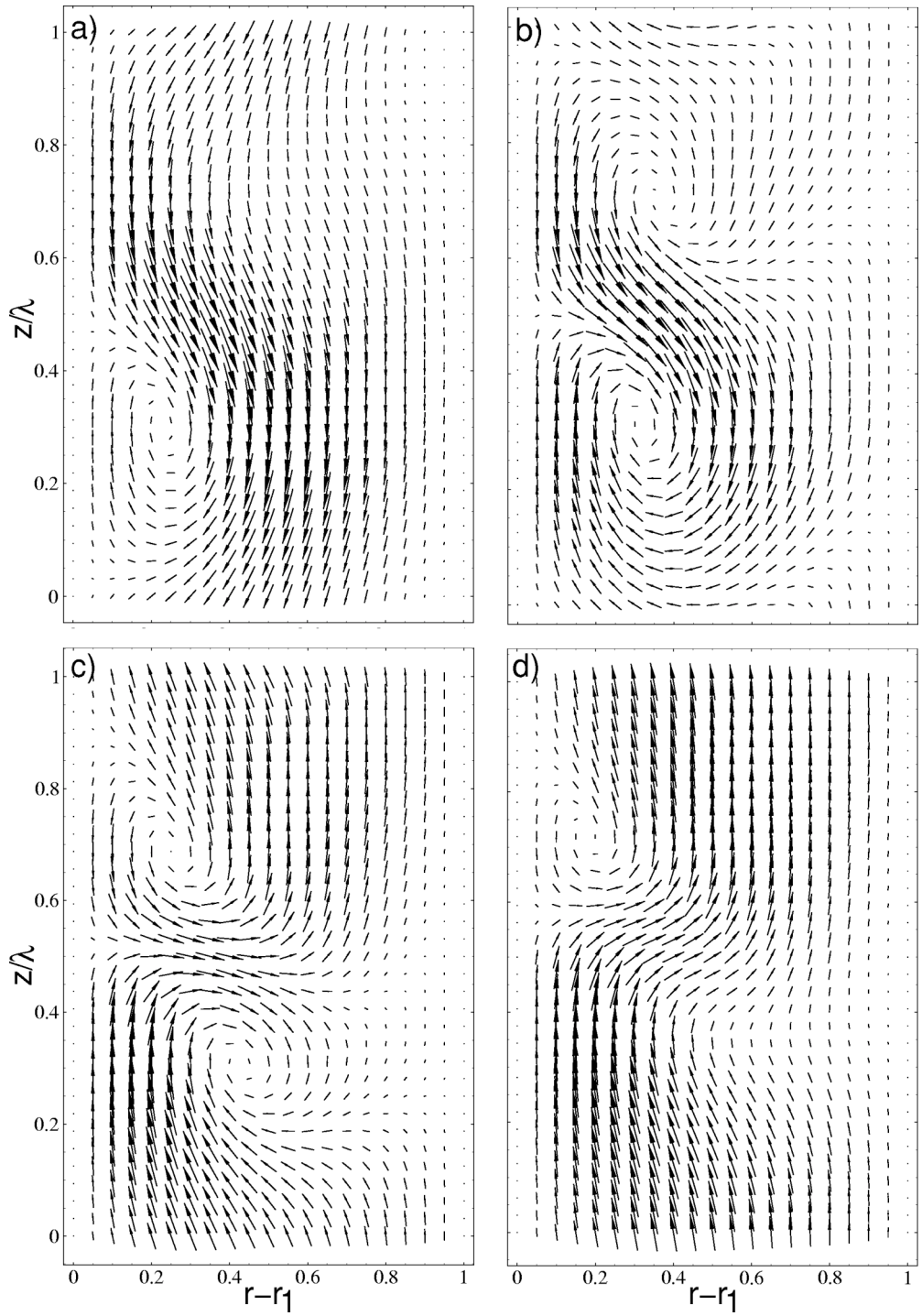

FIG. 12. Velocity field (u,w) of the L-SPI in an $r-z$ plane for Re$=-5$ (a), 0 (b), 5 (c), and 10 (d). Parameters are $\eta=0.5$, $k=3.927$, $R_1=120$, and $R_2=-100$.

$R_2=0$, $R_1=100$. This parameter combination lies well within the region E of Fig. 2 in which the TVF, L-SPI, and R-SPI are all stable at Re$=0$.

Switching on the through-flow one sees in Fig. 14(a) how the dominant modes of these vortex structures vary with Re. That SPI loses its stability for which the through-flow enforces a reversal of the phase propagation as in the case of counter-rotating cylinders (Fig. 10). Thus, also here the direction of the imposed through-flow is the preferred one for a stable SPI at large $|\mathrm{Re}|$. A spiral that has started at small $|\mathrm{Re}|$
to move against the through-flow becomes unstable when the latter becomes sufficiently strong to turn it back. On the other hand, a SPI remains stable at a large $|\mathrm{Re}|$ that keeps propagating into the preferred direction of the through-flow.

As in Fig. 10 the loss of stability takes place in the vicinity of the Reynolds number where the axial phase velocity

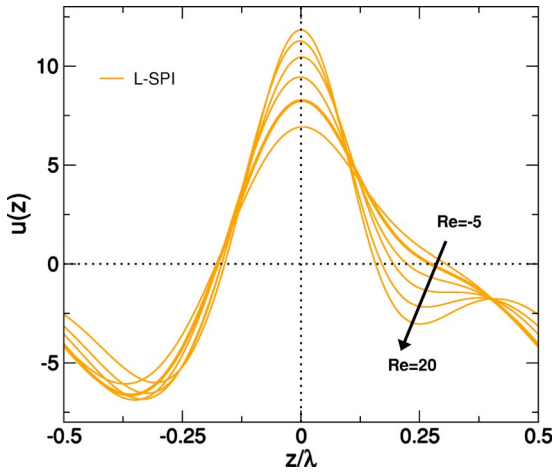

FIG. 13. (Color online) The effect of an external through-flow on the axial profiles of the radial velocity of the L-SPI. Lines show $u(z)$ at a midgap position for Re=−5 to Re=20 in steps of five. Thick one refers to Re=0. In each case the maximal radial outflow is chosen to lie at $z=0.5\lambda$. Parameters are $R_1=130$, $R_2=-100$, $\eta=0.5$, and $\eta=1.6$.

w_{ph} [Fig. 14(b)] of the respective SPI goes through zero. This happens in Fig. 14 for the $M=\pm 1$ SPI at $\mathrm{Re}\simeq\mp 6.4$. However, here we found the transition from the then unstable SPI to occur to the stable TVF solution [cf. arrows in Fig. 14(a)] rather than to the other stable SPI.

We have also briefly investigated the situation where the TVF solution was numerically eliminated (here, suppressing

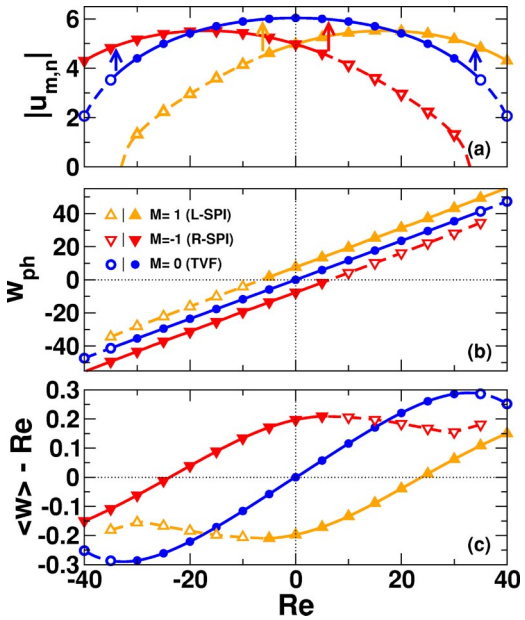

FIG. 14. (Color online) Infiuence of an external through-flow on vortex structures. (a) Primary Fourier amplitudes of the radial flow field at midgap for the $M=1$L- SPI ($u_{1,1}$), the $M=-1$ R-SPI ($u_{-1,1}$), and for the TVF ($u_{0,1}$). (b) Axial phase velocity $w_{ph}=\omega/k$. (c) Net mean axial flow $\langle w\rangle-\mathrm{Re}$. Full (dashed) lines with filled (open) symbols refer to stable (unstable) states. Arrows indicate transitions after loss of stability, see text for details. Parameters are $R_1=100$, $R_2=0$, $\eta=0.5$, and $k=3.927$.

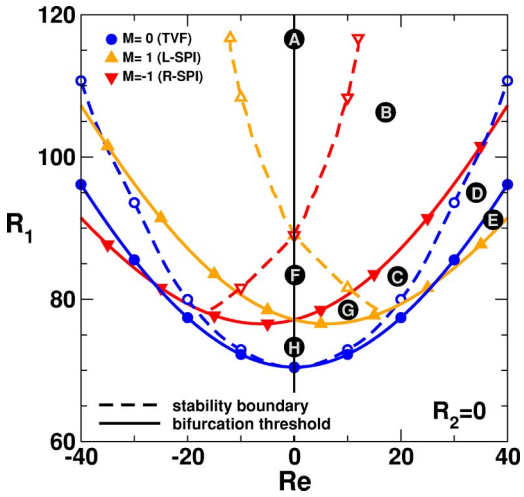

FIG. 15. (Color online) $R_1-\mathrm{Re}$ phase diagram of the TVF, R-SPI, and L-SPI for a stationary outer cylinder. Solid lines represent linear stability thresholds of the basic flow, i.e., bifurcation thresholds of the respective vortex solutions out of the combined CCF-APF solution. Dashed lines are stability boundaries of the vortex states. The phase diagram is symmetric under $\mathrm{Re}\rightarrow-\mathrm{Re}$. Parameters are $R_2=0$, $\eta=0.5$, and $k=3.927$.

Region	A	B	C	D	E	F	G	H
TVF	s	s	s	u	-	s	s	s
R-SPI	s	u	-	-	-	u	-	-
L-SPI	s	s	s	s	s	u	u	-

s: stable; u: unstable; -: nonexixtent.

$m=0$ modes of the u field at a midgap position turned out to be an efficient way to globally reduce the TVF towards zero). Also then, the SPI that is unfavored by the through-flow loses its stability. However, with the TVF being unavailable as a final state the transition occurs in this case to the favored SPI in a way that seems to be similar to the one described in Sec. IV A 1.

Without the above described numerically imposed mode restriction the TVF is stable for moderate through-flow rates while at sufficiently large |Re| SPIs are stable [26–28]. For our parameters the TVF decays at $\mathrm{Re}\simeq\pm 34$ into an $M=\pm 1$ SPI as indicated by arrows in Fig. 14(a).

For small through-flow the phase velocity w_{ph} and the net mean flow $\langle w\rangle$ vary roughly linearly with Re. The initial slopes $\partial w_{\mathrm{ph}}/\partial\,\mathrm{Re}$ and $\partial\langle w\rangle/\partial\,\mathrm{Re}$ are, for SPIs as well as for TVFs, roughly 1. However, at larger Re one sees in Fig. 14(c) that in particular $\langle w\rangle$ shows nonlinear corrections.

2. Phase diagram

Figure 15 shows the phase diagram of the TVF, R-SPI, and L-SPI for stationary outer cylinder in the control parameter plane spanned by Re and R_1. The *existence* range of the vortex states is bounded from below by the bifurcation threshold (full line in Fig. 15) of the respective vortex solution out of the combined CCF-APF basic state. These bifurcation thresholds result from a linear stability analysis of the

CCF-APF state [14]. The one for the TVF increases quadratically for small Re. Also the SPI threshold curves in Fig. 15 have a somewhat parabolic shape, but with minima shifted to finite Re. Thus, the threshold for the L-SPI first decreases for small positive Re but eventually increases at larger Re. By symmetry the R-SPI threshold curve in Fig. 15 is a mirror image under $\mathrm{Re}\rightarrow-\mathrm{Re}$ of the L-SPI threshold curve. Hence small through-flow destabilizes (stabilizes) the CCF-APF state against spirals that propagate into (against) the through-flow direction.

Note that for small Re in Fig. 15 the TVF bifurcates first when increasing R_1. But for sufficiently large Re the bifurcation sequence of the TVF and SPI is reversed since the bifurcation threshold for the TVF curves up faster with increasing Re than the one for the L-SPI. After their intersection stable SPIs bifurcate first out of the CCF-APF state. Hence, for example in region E of Fig. 15, only stable L -SPIs exist; in region D TVF exists, but only as an unstable solution and in region B they both exist bistably.

The dashed lines in Fig. 15 are stability boundaries of the vortex solutions. Different regions of Fig. 15 between various stability boundaries and bifurcation thresholds are identified with the respective stability properties of the vortex states in the caption of Fig. 15.

V. SUMMARY

We have numerically simulated vortex flow structures of different azimuthal wave numbers M in the Taylor-Couette system with counter-rotating as well as with corotating cylinders. In particular we have investigated the effect of an externally imposed axial through-flow on the spatiotemporal properties and on the bifurcation behavior of $M=1$ L spirals, $M=-1$ R spirals, and $M=0$ Taylor vortices.

To that end we first have determined for zero through-flow, $\mathrm{Re}=0$, the bifurcation surfaces of the appropriate order parameters characterizing SPI and TVF solutions over the R_1-R_2 control parameter plane of the inner and outer cylinder's Reynolds numbers. For the parameter combinations explored in this work these bifurcations out of the basic CCF state are forward, and their order of appearance determines the stability of the respective bifurcating vortex state: the vortex solution that bifurcates second is unstable. But it eventually becomes stable with increasing distance from the bifurcation threshold so that, e.g., for larger R_1 there is a large region in the R_1-R_2 plane with bistability of TVFs and SPIs. In particular the existence region of stable SPIs extends for axially periodic boundary conditions even to positive R_2 with corotating cylinders. Unstable solution branches were obtained by selectively suppressing destabilizing modes. Stable ribbons, i.e., nonlinear combinations of $M=\pm1$ spirals were not found.

Simulations of axially finite systems with rigid, nonrotating lids showed, in good agreement with experiments, how the stable existence range of SPIs is reduced by stationary Ekman vortices which suppress phase propagation at the two ends. Also the frequencies and wave profiles of the spiral vortices in the bulk of the numerical and experimental systems agreed well with each other. Spiral profiles obtained for periodic and rigid end conditions do not differ much. On the other hand, the respective frequencies differ basically by the Galilean contribution $\langle w\rangle k$ Here $\langle w\rangle$ is the net axial mean flow that the nonlinear Reynolds stresses of a spiral with axial wave number k sustains with axially periodic end conditions but not with impermeable ends.

Furthermore, we showed how the phenomenon of rigid body rotation of spirals can be understood quantitatively in terms of the passive advection dynamics of $M=\pm1$ vortex perturbations whose lines of constant phase are oriented obliquely to the azimuthal CCF. The onset spiral frequency is the mean rotation rate of the CCF, albeit weighted appropriately by the critical eigenfunctions with the consequence that the L-SPI as well as the R-SPI rotate in the same direction as the inner cylinder. The nonlinear SPI frequencies are typically smaller than the linear ones but do not deviate substantially from them.

A finite through-flow breaks the mirror symmetry between the L-SPI and R-SPI, and changes the structure of the SPI. The externally imposed axial pressure gradient does not just add the annular Poiseuille flow $w_{\mathrm{APF}}(r)$ to the axial velocity field. It modifies thr SPI structure, e.g.,the profiles of the radial flow in a characteristic way.

For $\mathrm{Re}=0$ L-SPIs propagate axially upwards and R-SPIs downwards. When they are initially stable they continue to coexist bistably for small through-flow. However, they are no longer mirror images of each other and their phase velocities differ by an amount $\propto\mathrm{Re}$. Then, with increasing $|\mathrm{Re}|$ that spiral loses its stability for which the through-flow enforces the phase velocity to change direction. Only that SPI is stable at a large $|\mathrm{Re}|$ that keeps propagating into the preferred direction of the through-flow. The other one is unstable at large $|\mathrm{Re}|$.

The SPI that loses stability upon reverting its propagation direction —i.e. the R-SPI (L-SPI) for positive (negative) Re—preferentially undergoes a transition to propagating TVF provided the latter is available as a *stable* vortex state. Otherwise the transition is to the then monostable L-SPI (R-SPI). Such a situation was explored in detail for negative R_2 where the TVF was unstable and for other parameter combinations where the TVF solution was eliminated numerically.

Also the situation where initially at $\mathrm{Re}=0$ all three vortex solutions are stable was elucidated for different R_1-R_2 parameter combinations and in more detail for a stationary outer cylinder, $R_2=0$. Here, a complete phase diagram was determined in the control parameter plane spanned by Re and R_1. We found that a small through-flow destabilizes (stabilizes) the basic CCF-APF state against spirals that propagate into (against) the through-flow direction. For sufficiently large Re the bifurcation sequence of TVFs and SPIs is reversed since the bifurcation threshold for TVF curves up faster with increasing Re than the one for the L-SPI. After their intersection stable SPIs bifurcate first out of the CCF-APF state. Then there opens up a region at sufficiently large positive Re in which only stable L-SPI but no Taylor vortices exist for stationary outer cylinder.

ACKNOWLEDGMENT

This work was supported by the DFG. We thank A. Schulz, J. Langenberg, and G. Pfister for communicating the experimental data referred to in this paper.

[1] *The Couette-Taylor Problem, Nonlinear Sci. Today* **4**, 1 (1994).
[2] P. Chossat and G. Iooss, *The Couette-Taylor Problem* (Springer, Berlin, 1994).
[3] E. R. Krueger, A. Gross, and R. C. DiPrima, J. Fluid Mech. **24**, 521 (1966).
[4] H. A. Snyder, Phys. Fluids **11**, 728 (1968).
[5] C. D. Andereck, S. S. Liu, and H. L. Swinney, J. Fluid Mech. **164**, 155 (1986).
[6] W. F. Langford, R. Tagg, E. Kostelich, H. L. Swinney, and M. Golubitsky, Phys. Fluids **31**, 776 (1988).
[7] R. Tagg, W. S. Edwards, H. L. Swinney, and P. S. Marcus, Phys. Rev. A **39**, 3734 (1989).
[8] W. S. Edwards, in *Instability and Transition*, edited by M. Y. Hussaini (Springer, Berlin, 1990), Vol. II p. 408.
[9] A. Schulz and G. Pfister, in *Physics of Rotating Fluids*, edited by C. Eghers and G. Pfister, Lecture Notes in Physics, Vol. 549 (Springer, Berlin, 2000), p. 37; and (unpublished).
[10] J. Antonijoan, F. Marquès, and J. Sánchez, Phys. Fluids **10**, 829 (1998).
[11] P. Büchel, M. Lücke, D. Roth, and R. Schmitz, Phys. Rev. E **53**, 4764 (1996).
[12] Th. Gebhardt and S. Crossmann, Z. Phys. B: Condens. Matter **90**, 475 (1993).
[13] A. Meseguer and F. Marques, J. Fluid Mech. **455**, 129 (2002).
[14] A. Pinter, M. Lücke, and Ch. Hoffmann, Phys. Rev. E **67**, 026318 (2003).
[15] R. Raffai and P. Laure, Eur. J. Mech. B/Fluids **12**, 277 (1993).
[16] J. B. Swift, K. L. Babcock, and P. C. Hohenberg, Physica A **204**, 625 (1994); R. J. Deissler, Phys. Rev. E **49**, R31 (1994); M. Lücke and A. Szprynger, *ibid.* **55**, 5509 (1997).
[17] K. L. Babcock, G. Ahlers, and D. S. Cannell, Phys. Rev. E **50**, 3670 (1994); A. Szprynger and M. Lücke, *ibid.* **67**, 046301 (2003).
[18] S. T. Wereley and R. M. Lueptow, Phys. Fluids **11**, 3637 (1999).
[19] C. W. Hirt, B. D. Nichols, and N. C. Romero, *SOLA—A Numerical Solution Algorithm for Transient Fluid Flow* (Los Alamos Scientific Laboratory of the University of California, LA-5852, 1975).
[20] R. Peyret and T. D. Taylor, *Computational Methods in Fluid Flow* (Springer, Berlin, 1983).
[21] A. Recktenwald, M. Lücke, and H. W. Müller, Phys. Rev. E **48**, 4444 (1993).
[22] M. C. Cross and P. C. Hohenberg, Rev. Mod. Phys. **65**, 851 (1993).
[23] In Fig. 5(a) of Ref. [24] the quantity labeled "axial mean flow $-\langle w \rangle$" is too small by a factor of 2π.
[24] Ch. Hoffmann and M. Lücke, in *Physics of Rotating Fluids*, Lecture Notes in Physics 459, edited by C. Egbers and G. Pfister (Springer, Berlin, 2000), p. 55.
[25] W. S. Edwards, R. P. Tagg, B. C. Dornblaser, and H. L. Swinney, Eur. J. Mech. B/Fluids **10**, 205 (1991).
[26] K. Bühler and F. Polifke, in *Nonlinear Evolution of Spatio-temporal Structures in Dissipative Continuous Systems*, edited by F. Busse and L. Kramer (Plenum, New York, 1990), p. 21.
[27] R. M. Lueptow, A. Docter, and K. Min, Phys. Fluids A **4**, 2446 (1992).
[28] A. Tsameret and V. Steinberg, Phys. Rev. E **49**, 4077 (1994).